Kovove Mater. 59 2021 119–130
DOI: 10.4149/km_2021_2_119

Comparison of the effect of EB and LB surface treatment on structural characteristics of IN 713LC superalloy

E. Švábenská[1]*, V. Horník[1], S. Fintová[1,2]

[1]*Institute of Physics of Materials, Czech Academy of Sciences, Žižkova 22, 616 00 Brno, Czech Republic*
[2]*CEITEC IPM, Institute of Physics of Materials, Czech Academy of Sciences, Žižkova 22, 616 00 Brno, Czech Republic*

Received 11 February 2021, received in revised form 25 February 2021, accepted 16 March 2021

Abstract

Damage and oxidation resistance are properties characterizing Ni-based superalloys. However, besides the alloy composition, the mentioned properties depend on structural features such as grain and precipitates size. Surface structure refinement via laser beam (LB) and electron beam (EB) was performed on IN 713LC superalloy. The influence of both the treatments on material microstructure, chemical composition, microhardness, and oxidation resistance was examined. Both the treatments resulted in a refined structure of the remelted zone. A homogeneous 30–43 μm thick remelted zone was created by EB, while a non-homogeneous (semi-circular track) remelted zone (22–86 μm) was created by LB. EB treatment resulted in higher surface roughness; however, a smaller amount of cracks on the treated sample surface was observed compared to the LB treatment. An increase of surface microhardness by 38 % compared to the as-received material was reached regardless of the used treatment method. The impact of the treatment on oxidation resistance was studied after exposure to 800 °C for 24, 48, 72, and 96 hours in the ambient air. The created oxide layer consisted of internal Al_2O_3 and external $Cr_2O_3 + NiCr_2O_4$ layer. The oxide layer thickness differs in time; however, comparable oxide layer thickness was measured on all samples after 96 hours of oxidation.

Key words: IN 713LC, electron beam, laser beam, microstructure, surface treatment, oxidation

1. Introduction

Nickel-based superalloys are structural materials suitable for high-temperature applications in many industry fields, e.g., automotive, aerospace, and power industry. The components made from this class of alloys are characterized by excellent mechanical and corrosion properties at high temperatures. One of the most frequently used cast Ni-based superalloys is IN 713, and its low carbon variant IN 713LC. The microstructure of IN 713LC superalloy is created by a matrix of γ phase with high chromium content, strengthening γ' precipitates, and a small number of carbides. Compared to other Ni-based superalloys, the advantage of the IN 713LC is its possible application in as-cast conditions without further heat treatment [1–8]. High content of chromium and aluminum in Ni-based superalloys allows forming a layer consisting of Cr_2O_3 and/or Al_2O_3 oxides in a corrosive environment. The layer ensures high oxidation resistance even at high temperatures in the air [9, 10]. Since the superalloy's oxidation resistance under loading is one of its most valued properties, additional coatings and thermal barriers and their influence on the IN 713 superalloy mechanical properties, especially fatigue resistance, are studied [3, 4, 6–8].

One of the methods of controlling material mechanical properties is grain size. Grain refinement usually leads to mechanical properties improvement, especially strength, hardness, and fatigue resistance. Ni-based superalloys castings are generally characterized by large grain size (units of millimeters). Surface grain refinement can be an appropriate method to improve material resistance against crack initiation under loading. Besides mechanical treatment, surface remelting and solidification under a high cooling rate

---

*Corresponding author: e-mail address: svabenska@ipm.cz

Table 1. Chemical composition of IN 713LC measured by GDOES (in wt.%)

Element	C	Cr	Al	Mo	Nb	Ti	Fe	Zr	Mn	Si	B	Ni
Content	0.06	12.39	6.42	4.07	2.07	0.64	0.02	0.04	0.06	0.04	0.01	Bal.

is a method to obtain a fine-grained surface layer. A laser beam (LB) and electron beam (EB) surface treatment usually used for welding [11–13], forming [14], surface texturing [15], or quenching [16] are methods how to change the material surface structure and influence its chemical composition (elements redistribution). The structural changes occur due to fast-heating, melting, even some elements evaporation, followed by rapid solidification and cooling of the surface remelted layer [17, 18]. Cooling rate and various solid-state transformation reactions influence the development of the remelted zone's microstructure, consisting of fusion zone (FZ) and heat-affected zone (HAZ).

Refinement of the surface layer structure of Ni-based superalloys due to the beam treatment was analyzed in a few studies. Depending on the used parameters, planar, cellular, columnar, or equiaxed dendritic structure in the FZ was observed [11, 17, 19]. Also, the secondary γ' precipitates size change was documented, depending on the used beam parameters, for RR1000 [20], IN 738LC [18], and IN 713C [11, 21]. A higher cooling rate was always connected with finer microstructure. Besides the structure, the beam treatment parameters, especially the cooling rate, also influence the residual stresses and their relaxation via cracks formation [11, 13, 22–25]. The liquidation cracks were shown to propagate along grain boundaries and grain interior, mainly in HAZ. In contrast, the solidification cracks are formed in FZ during solidification and follow grain boundaries and interdendritic areas. Since the temperature in the center of the weld pool can be close to the alloy's boiling point, another aspect of the remelting of the treated material is the potential vaporization of alloying elements [26]. Consequently, a change in the elemental composition of the treated Ni-based superalloys and steel surface was observed in [27–29].

The present study aims to analyze and compare the influence of LB and EB treatment (remelting the material to the depth of approximately 50 µm) on the surface of IN 713LC Ni-based superalloy. The surface morphology, final microstructure, chemical composition, and microhardness reached due to the surface beam treatment will be correlated to the material oxidation resistance.

2. Experimental material and methods

To determine the influence of the surface beam treatment, the as-received (AR) samples with a polished surface with LB and EB treated samples' structural and mechanical characteristics were compared.

2.1. Material

Conventionally used polycrystalline IN 713LC superalloy provided by PBS Velká Bíteš a.s. (Velká Bíteš, Czech Republic) in the form of rods with a diameter of 18 mm was used as the experimental material. The casting temperature was 1360 ± 10 °C, and no heat treatment was applied after the casting.

The chemical composition of the experimental material before surface treatment was analyzed by a Glow discharge optical emission spectrometry (GDOES) using the *GD-Profiler 2 instrument* with the *Quantum*$^{\mathrm{TM}}$ *XP software* operating at a frequency of 13.56 MHz. The nominal chemical composition of the IN 713LC obtained by GDOS is given in Table 1.

The metallographic examination was carried out by light optical microscopy (LM-Olympus GX51) and scanning electron microscopy (SEM – Tescan LYRA 3 equipped with an X-Max80 EDS detector). Microstructural analysis was performed in the cut perpendicular to the AR rod axis. Perpendicular cuts were ground and polished. To reveal the microstructure, the etchant consisting of 40 ml HNO_3 and 30 ml HF was used. The electrolytic etching was used for the visualization of the cuboidal shape γ' precipitates. For this purpose, the solution of 100 ml H_2SO_4 and 200 ml H_2O at 5 V for 10 s at laboratory temperature (23 ± 2 °C) was used.

The AR alloy's microstructure consists of coarse dendritic grains with an average size of about 1 mm (measured by the linear intercept method on 10 areas) (Fig. 1a). A high volume fraction (approx. 53 %) of cuboidal shape strengthening γ' precipitates with an average size of 0.75 µm (Fig. 1b) is homogeneously distributed in the γ matrix. The casting defects with a maximum size of 0.4 mm were observed in the material microstructure.

The cylinders with a length of 10 mm were cut by an electric discharge machine from the delivered AR pre-cast rods (Fig. 2). The cylinders' top surfaces (the plane perpendicular to the rods axis) were ground and polished (1 µm diamond paste using ethanol as a lubricant) before surface beam treatment.

2.2. Structural and surface analysis

Treated surface morphology, microstructure below the surface, and the chemical composition of the

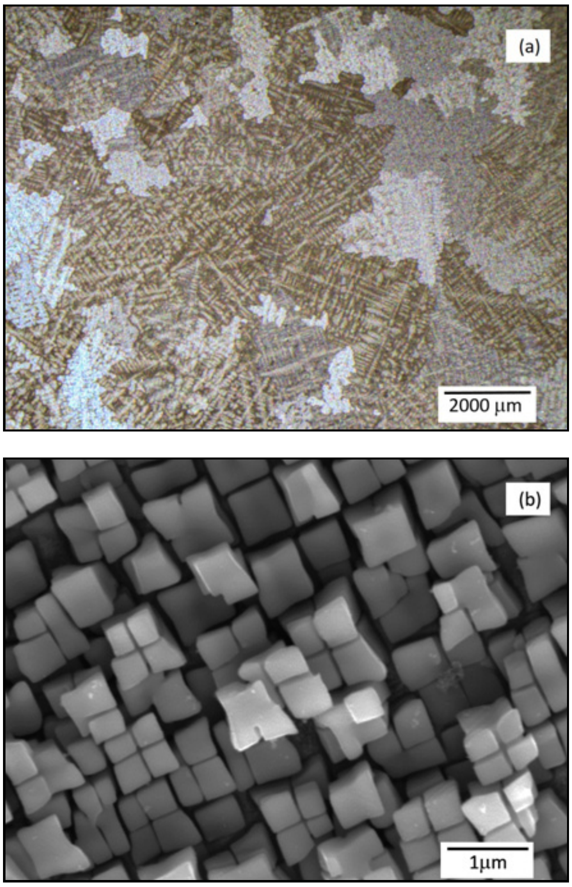

Fig. 1. The dendritic structure of IN 713LC, LM (a); the detail of the cuboidal shape γ' precipitates, SEM (b).

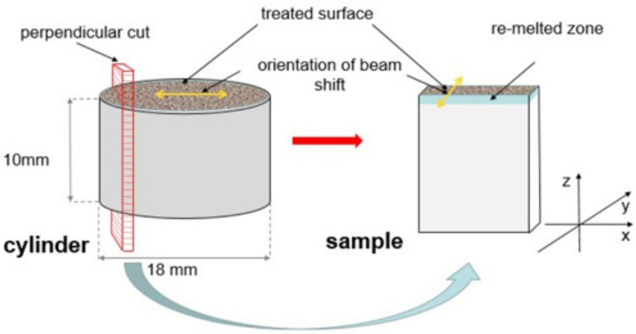

Fig. 2. The sample preparation scheme and location of surface treatment.

treated surface, as well as the microstructural and chemical composition changes, were examined using SEM, including energy dispersive spectroscopy (EDS).

Olympus LEXT OLS3100 confocal microscope with AFM module was used to visualize the 3D morphology of the treated surface. The surface morphology was characterized by 3D visualization and roughness measurement.

X-ray diffraction (XRD) using X'Pert diffractometer, with Bragg-Brentano geometry and CoKα radiation with qualitative analysis by the *HighScore® software* and the *JCPDS PDF-4 database* was used for the analyses of phase composition of the treated surface layer (remelted zone) and of the layer after the oxidation. For quantitative analysis, HighScore plus® with Rietveld structural models based on the ICSD database was applied. Grazing incidence measurements (GI-XRD) were yielded with a fixed detector in the parallel beam with tilt $\alpha = 0.5°–5°$.

The subsurface microhardness (HV0.01) in the treated layer was measured using the Vickers standard method (ISO 6507-1) on the polished cuts perpendicular to the treated surface plane. LECO LM 247 AT hardness tester was used for microhardness measurement. The average value was calculated from 5 measurements.

2.3. Surface treatment

Trumpf TruDisk 8002 laser with Scanlab Intelii-WELD scanning head in cooperation with New Technologies – Research Centre (University of West Bohemia, Pilsen, Czech Republic) was used for LB treatment. The wavelength of 1030 nm and the diameter of 840 µm were applied. LB treatment was performed in a vacuum chamber evacuated to a pressure of 0.1 bar and then filled up by nitrogen gas to a pressure of 1.3 bar. The laser power of 200 W with a feed rate of 40 mm s^{-1} for the surface treatment was used. Track shift was 0.3 mm, and one repetition of the beam tracking for the surface was used.

EB treatment was performed using K26 15-150 ProBeam facility in cooperation with NETME Centre (Institute of Materials Science and Engineering, Brno University of Technology, Czech Republic). The treatment was carried out under vacuum (1.4×10^{-5} mbar). The voltage of 120 kV and a current beam of 10 mA at the frequency of 1000 Hz was used for the surface treatment. The feed rate was 35 mm s^{-1}. Also, in this case, only one repetition of the beam tracking for the surface was used.

EB and LB treatment parameters were chosen to remelt the surface layer to a depth of approximately 50 µm.

2.4. Oxidation tests

Oxidation tests were performed on the AR, EB, and LB treated samples with a thickness of 2 mm, cut by an electric discharge machine from prepared cylinders after treatment (Fig. 2). The samples were annealed in alumina crucibles at a temperature of 800 °C for 24, 48, 72, and 96 hours in the air of ambient pressure. After the testing time, the samples were removed from the furnace

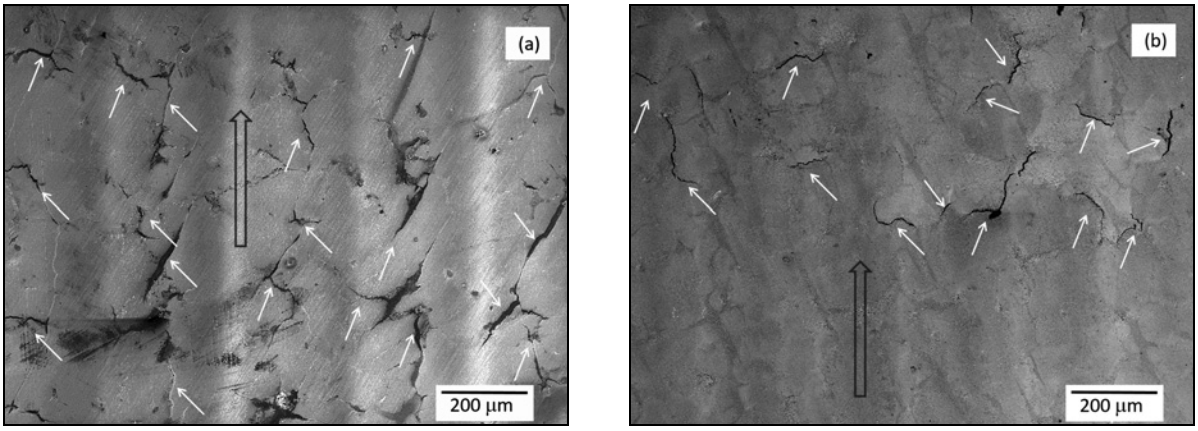

Fig. 3. The SEM micrographs of LB treated surface (a); EB treated surface (b). The black arrow marks the direction of the beam tracking, and the white arrows indicate the cracks.

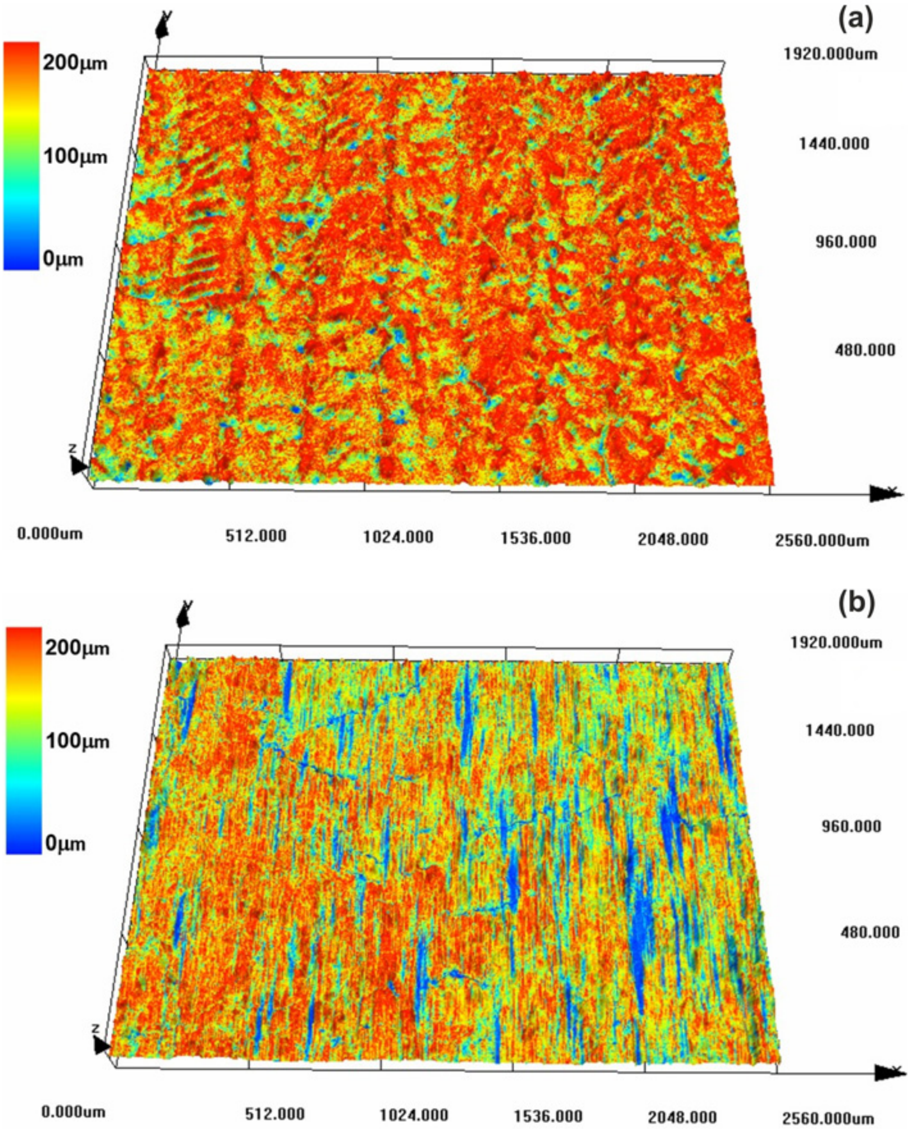

Fig. 4. 3D images of the surface of LB (a) and EB (b) samples.

and cooled freely in the air to laboratory temperature.

After the test, the samples were molded, ground, and polished, and the oxide layer was analyzed using SEM and EDS. The oxide layer was covered by gold before the samples were molded into the conductive resin.

3. Results and discussion

3.1. Surface morphology

Surfaces of both the samples after beam treatment exhibit waviness, and numerous cracks were observed by SEM (Fig. 3). A higher amount of cracks on the LB treated surface (Fig. 3a) than on the EB treated sample (Fig. 3b) was observed visually. No correlation between the direction/shape of the present cracks and the beam tracking was observed, regardless of the used surface treatment method. On the other hand, 3D surface morphology visualization (Fig. 4) revealed the correlation of the surface morphology with the beam tracking. For both treated surfaces, characteristic features in a vertical direction (beam track direction) were detected.

Even though a higher number of cracks was present on the LB treated sample, the EB sample (Fig. 4b) shows higher roughness of the analyzed area in comparison with the LB sample (Fig. 4a). The arithmetic average roughness (*Ra*) for the inspected area ($2560 \times 1920\,\mu m^2$) of the LB sample was 9.33 and 10.334 for the EB sample. The value of the maximum height of the profile on the inspected area (*Rz*) for the LB sample was 99.58, while for the EB sample, it was 178.89. Nevertheless, a smaller number of cracks in the case of the EB sample was observed by SEM (Fig. 3b); however, according to the morphology 3D visualization, the cracks on the EB sample (Fig. 4b) seem to be much deeper than in the case of the LB sample (Fig. 4a).

The creation of the observed cracks is a consequence of beam treatment. As a result of the heat introduction during treatment, the remelted surface layer creates. Due to the thermal gradient between the remelted surface layer and base material, rapid solidification occurs. Relaxation of the introduced residual stresses results in the solidification crack formation [22–24].

More cracks created in the LB treated sample can indicate more pronounced cooling of the surface comparing to the EB treated sample. On the other hand, a smaller amount of cracks serving as the stress relaxation areas on EB treated sample results in their higher depth when compared to the higher amount of cracks, assuming the relaxation of comparable residual stresses.

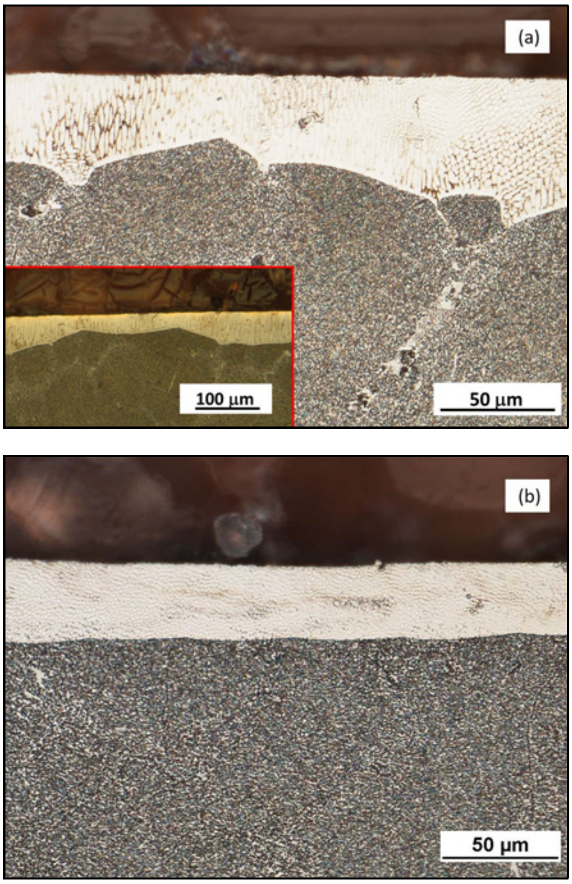

Fig. 5. The remelted zone of treated samples LB (a) and EB (b), LM.

3.2. Microstructure

The remelted zones remaining after EB and LB treatment were examined in the whole length of the sample cross-cuts. The typical microstructure is shown in Fig. 5. The depth of the influenced surface layer was chosen based on the assumption that the defects below 50 µm potentially created in the treated layer can be considered non-damaging from the mechanical point of view (crack initiation).

The LB sample's remelted zone exhibited a non-homogeneous character (semi-circular track) (Fig. 5a). The average thickness of the zone was 50 µm (from 22 to 86 µm), according to the position on the semicircular track caused by the laser beam. On the other hand, the remelted zone exhibited similar thickness in the EB sample case (Fig. 5b). The average value of the zone thickness was 37 µm (interval between 30 and 43 µm). The microstructure of the treated samples' remelted zone differs from the microstructure of the base material (Figs. 5 and 6). The EB sample's remelted zone consisted only from FZ, while in the case of LB sample also a thin HAZ (approximately 2–4 µm) was observed between FZ and the base material.

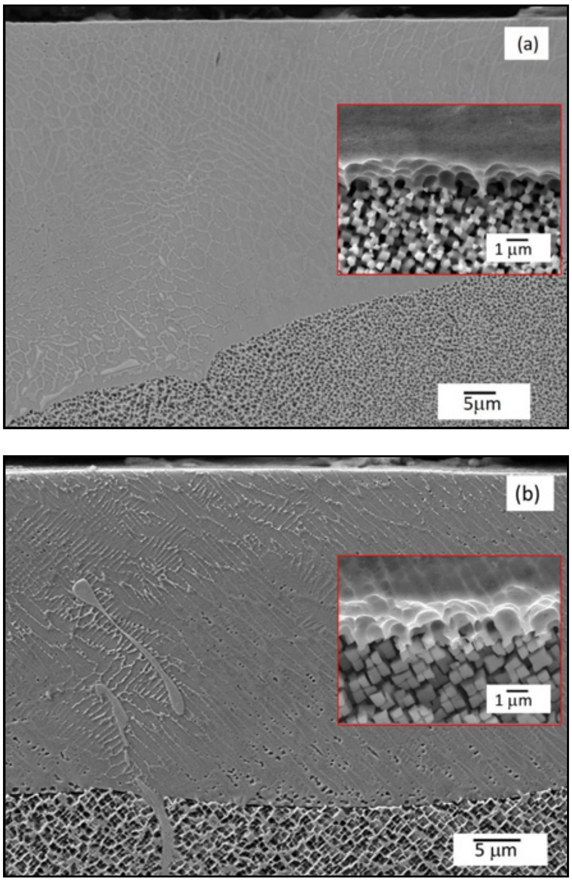

Fig. 6. Changes in microstructure of remelted layer of LB sample (a) and EB sample (b) supplemented with detail of boundary between remelted layer and original material (electrolytic etching), SEM.

The dendritic microstructure was characteristic to be obtained after both treatments. Depending on the solidification conditions, the microstructure changed from cellular-dendritic (LB) (Fig. 6a) to columnar (EB) (Fig. 6b).

Different shapes of dendrites in the treated samples' remelted zones are related, especially, to the cooling rate of material in FZ, various positions in the hemispherical trace of the beam, and the original arrangement of the basic material as-cast structure. The FZ's homogeneous thickness and columnar microstructure after EB treatment indicate a more homogeneous heat distribution within the material during treatment (Fig. 6b). A low heat gradient resulted in columnar microstructure creation. On the other hand, laser pulsing resulted in a non-homogeneous distribution of heat, resulting in a zone with a semicircular character observed for LB treated sample (Fig. 6a). Due to the heterogeneous heat distribution, the microstructure in the FZ of the LB treated sample is heterogeneous (mostly cellular-dendritic, however, also columnar areas were observed). Since the same remelted zone thickness was required, different beam conditions for electron and laser had to be set; especially the beam focus influencing the path's thickness and the resulting area of treated material liquidation. The observed microstructural changes are in agreement with [17, 21]. A similar observation was also published by Liang and Wang after laser surface remelting of single-crystal SRR99 superalloy [30].

The observed differences in the dendritic structures of the EB and LB remelted zones correspond to the cracks observed on the surface. A smaller amount of cracks was observed in the homogeneously thick remelted zone after EB treatment, and the heterogeneously solidified zone after LB treatment exhibited a higher amount of cracks.

Contrary to the base material, both samples after surface treatment exhibited a significant refinement of the cuboidal secondary γ' precipitates in the FZ and also HAZ in the case of the LB sample. Figures 6a and 6b manifested distribution of well visible cuboidal secondary γ' precipitates in the original material and dendritic structures in remelting layer without visible cuboidal secondary γ' precipitates. According to microscopy observation, the size of the secondary γ' precipitates in the remelted FZ was estimated on the scale of tens of nm. Nevertheless, calculation from the broadening of $\{110\}$ superlattice XRD peak determined the size of precipitates as a mixture of fine (20–60 nm) and coarse (> 350 nm) γ' precipitates in the surface remelted layer of both the samples. In comparison, the average size of γ' precipitates in the AR state was around 750 nm.

Secondary precipitates refinement was also observed in other works. Lachowitz and Dudziński [21] documented very fine secondary γ' precipitates in the Inconel 713C remelted zone formed by Gas Tungsten Arc (GTA) fusion (by SEM in HAZ and by transmission electron microscopy in FZ). Different sizes of secondary γ' precipitates obtained during various preweld heat treatment conditions for Inconel 738 superalloy were also mentioned in the work of Egbewande et al. [12], reporting the size reduction of γ' precipitates from 400–10000 nm for standard treatment to about the size of approximately 100 nm for the preweld heat treatment. The dendritic structure changes and the precipitates refinement are connected mainly with the cooling rate after the FZ remelting. As a quite high-speed cooling happened, the diffusion process was inhibited. Consequently, precipitates coarsening was not allowed, and only fine precipitates in the FZ and eventually HAZ microstructure were present after surface treatment.

Locally, the cracks were observed in the remelted zones after both treatment methods on the samples cross-cuts. The cracks started at the surface, grew perpendicularly through the remelted zone, and continued to the base material. The cracks occurred and

Table 2. Chemical composition of the samples surface, EDS (in wt.%)

Sample	Al	Ti	Cr	Zr	Nb	Mo	Ni
AR	6.28	0.68	11.21	0.02	2.24	4.17	Bal.
EB	5.88	0.70	11.58	0.08	1.98	4.05	Bal.
LB	7.68	0.79	11.15	0.31	2.48	4.02	Bal.

usually initiated in the interdendritic areas and exhibited the tendency to propagate along the grain or dendrite boundary through the whole FZ into the base material. Based on their character, the cracks can be identified to be created due to the solidification and relaxation of residual stresses.

A low thickness of the surface-treated layer was chosen to ensure the layer free of discontinuities and defects. However, the present cracks can act as the stress concentrators resulting in component fatigue properties deterioration [4–7]. On the other hand, the subsequent treatment ensuring introduced stresses relaxation should result in a crack-free layer improving material resistance against the fatigue crack initiation due to the strengthening via microstructure refinement.

3.3. Chemical and phase composition

LB and EB treatment changed the chemical composition of the surface layer of the superalloy. Compared with the base material, the surface of samples after treatment exhibits some changes in the concentration of all elements listed in Table 2. The aluminum shows the most remarkable visible change in concentration. In the case of EB treatment, the concentration of Al decreases. Compared to the untreated sample AR, the concentration of Al for the sample after LB treatment increases. There are several possible reasons why these changes occur. The treatment conditions and applied protection atmosphere (nitrogen for LB and vacuum for EB treatment) are different. Aluminum has the highest saturated vapor pressure and evaporation rate compared to other elements in IN 713LC Ni-based superalloy. The combination of these conditions can lead to different concentrations of Al and other elements.

Similar changes in the concentration of some of the alloying elements were described in [27–29]. Increasing content of Al, Si, Cr, Fe, and W, together with the decreasing concentration of Mo, Co, and Ni in an ablated area in the case of Hastelloy X superalloy after femtosecond laser beam interaction, was observed by Petronic et al. [27]. The authors explained the effect by carbide formation. In the present study, a small number of carbides in the remelted zone were observed. However, as the carbides were distributed continuously from the AR material to the remelted zone, they can be identified as primary carbides created during the component solidification and not secondary ones formed due to the remelting of the surface layer.

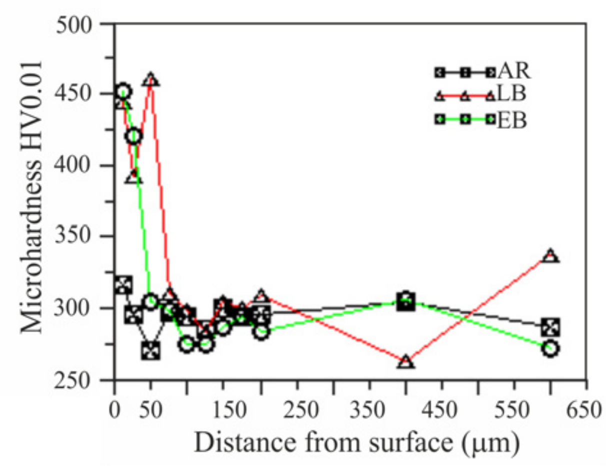

Fig. 7. The dependence of microhardness on the distance from the surface of the sample.

3.4. Microhardness

The dependence of microhardness on the distance from the surface of the sample is shown in Fig. 7. AR sample shows a uniform microhardness of approximately 300 HV0.01, regardless of the distance from the surface. Surface treatment resulted in a significant increase of the microhardness by almost 50 %, regardless of the used technique. The treated samples' microhardness profile corresponds to the remelted zones depth, taking into account the changing depth of the remelted zone in the specific area (semi-circular track) on the LB treated sample (Fig. 5). The microhardness increase is connected to the microstructural changes – dendritic structure refinement and the secondary γ' precipitates refinement.

The increase of the microhardness agrees with Petronic et al. [27], who observed increasing microhardness of the treated surfaces of Ni-based superalloys after laser beam machining of Hastelloy X and Nimonic 263. Petronic et al. [27] explained the microhardness increase by the formation of carbides in the remelted zone. The creation of fine carbides in the present study was observed as well. The volume fraction of the primary and the fine carbides was not

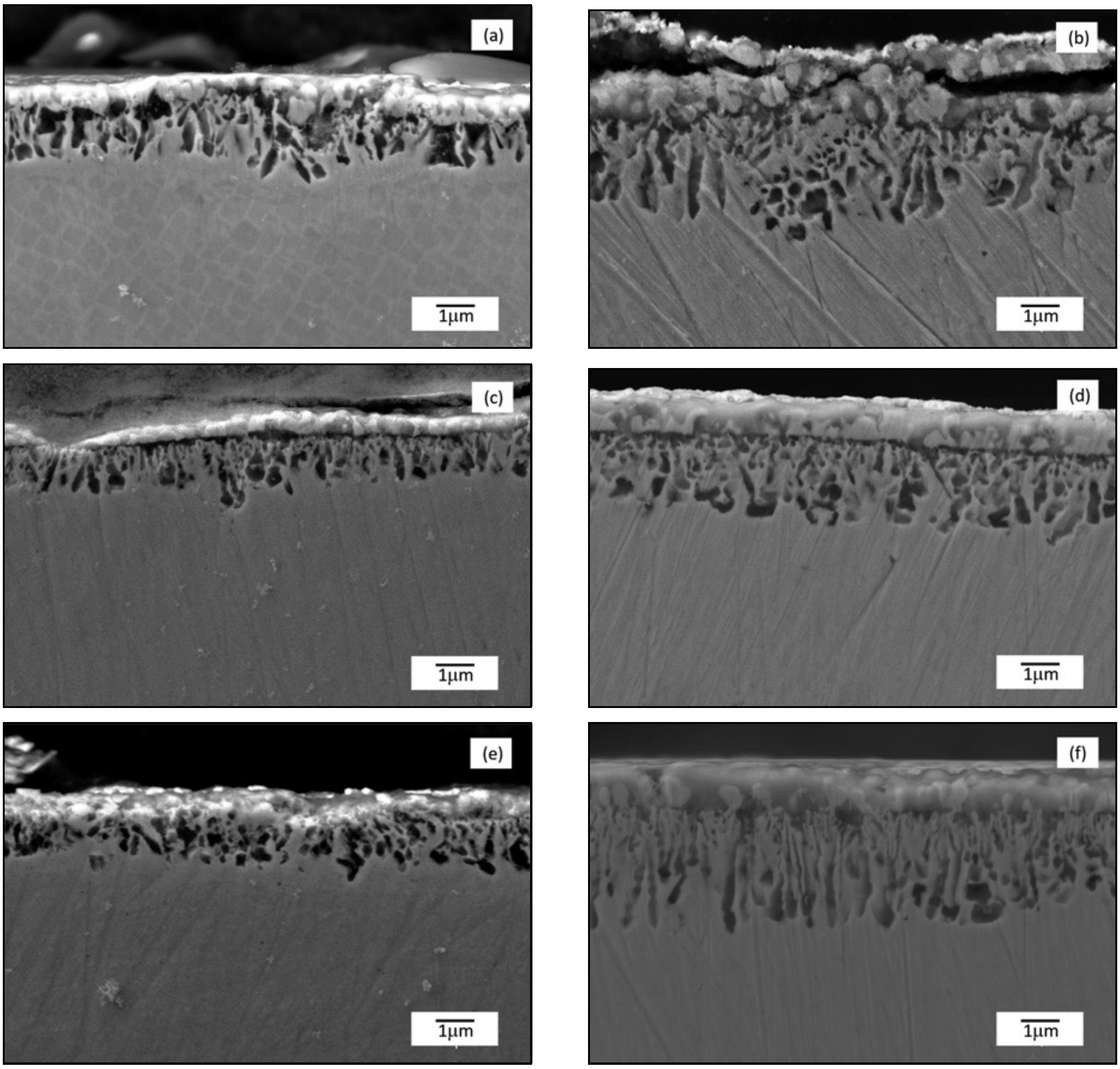

Fig. 8. The cross-section of the samples after oxidation test at 800 °C for 24 and 96 hours: AR – 24 hours (a), AR – 96 hours (b), EB – 24 hours (c), EB – 96 hours (d), LB – 24 hours (e), and LB – 96 hours (f).

analyzed. However, as the main factor influencing the microhardness of the surface, the microstructure refinement was identified in the present study.

From the mechanical point of view, the refined surface layer with increased microhardness should be more resistant against the cracks initiation. If the crack is created, another two aspects could retard its propagation: i) residual stresses can be beneficial for the crack closure and/or ii) the softer core of the treated product can stop the crack growth via high energy consumption for its growth. However, the influence of the introduced residual stresses decreases at elevated temperatures due to the material relaxation. The elevated temperatures enhance oxygen diffusion, resulting in brittle oxide layer creation on the fractured surfaces and crack growth facilitation. Thus, the effect of the surface remelted layer characteristic by the fine microstructure has to be analyzed additionally.

3.5. Oxidation

Figure 8 compares micrographs for all materials under investigation after an exposure time of 24 and 96 hours to the oxidation atmosphere. The cross-section showed an oxide layer after 24 hours (Fig. 8a) and 96 hours (Fig. 8b) on samples AR. The increase in the thickness of the main internal layer after 96 hours is visible. The longer time interval (96 hours, Fig. 8d) increases the thickness of both external and internal oxide layers on the sample EB. The thickest internal layer was created on the LB sample after 96 hours

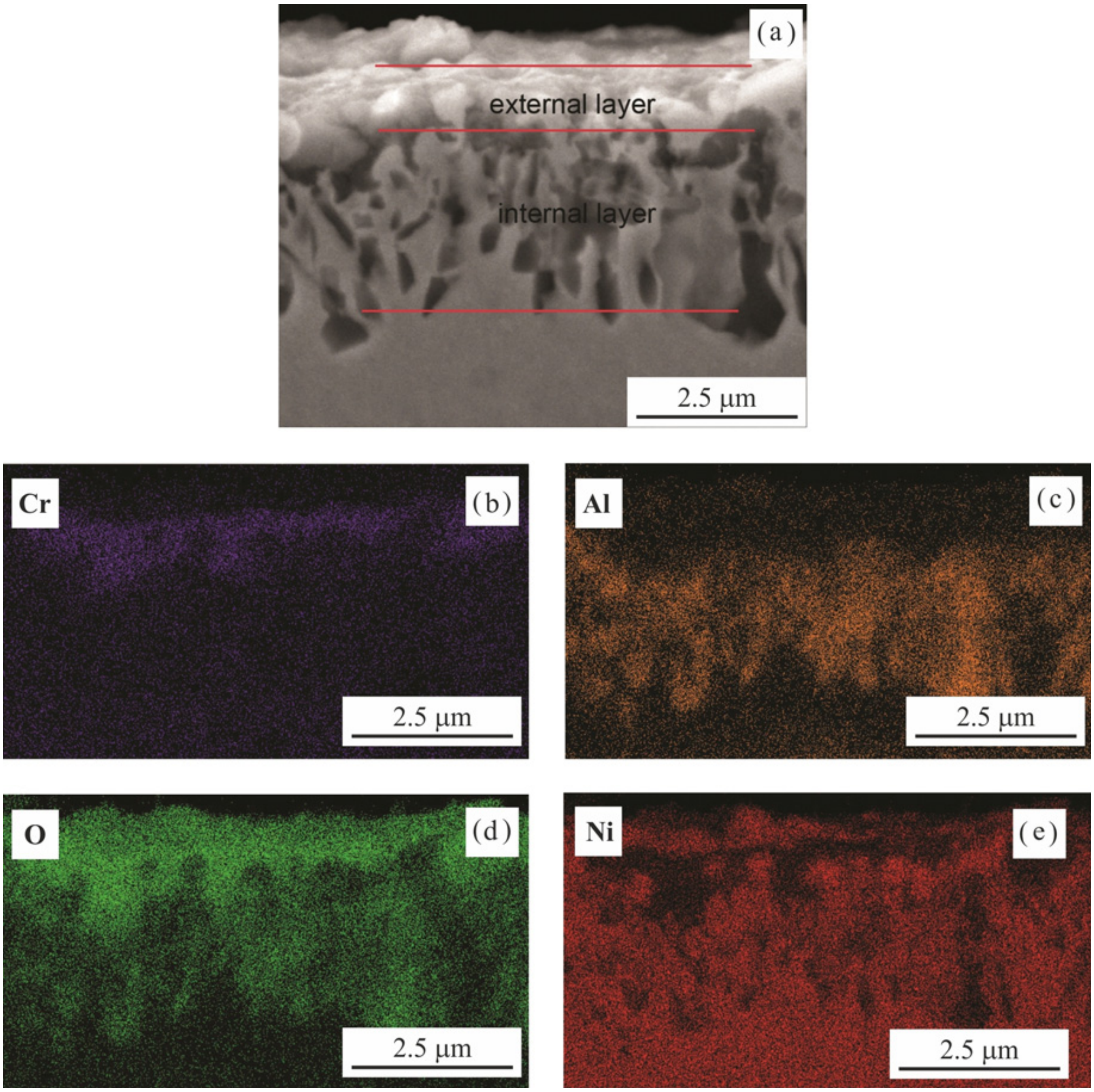

Fig. 9. Distribution of elements of the external and internal oxide layer on the EB treated sample after oxidation test at 800 °C for 72 hours.

(Fig. 8f), as shown in comparing the created oxide layers. The thickness of the external oxide layer in time 24 hours is comparable for all samples (AR – Fig. 8a, EB – Fig. 8c, LB – Fig. 8e). The thickness of the oxide layer was relatively uniform on individual samples.

EDS mapping revealed differences in the distribution of the elements. EDS mapping images showing the elemental distribution in the EB treated sample after 72 hours of oxidation are shown in Figs. 9a–h. The oxide layer created on the samples' surface consisted of two parts (Fig. 9a) – the external and internal layer (darker layer growing into the material), containing different types of oxides. The distribution of the elements was the same for all samples; only the thicknesses of surface external and subsurface internal layers were varying according to the type of surface treatment and duration of oxidation test.

The concentration of alloying elements and test temperature performed an essential role in creating an oxide layer. Three types of possible preferential oxide layers could be expected for Ni-Cr-Al systems [9]:

1. NiO layer with sub-layers containing Cr_2O_3 and/or Al_2O_3,
2. layer of Cr_2O_3 with internal sub-layers of Al_2O_3,
3. layer consisting only of Al_2O_3.

The XRD analysis of the external layer created on all the analyzed samples (lighter compact layer on the surface) revealed the presence of Cr_2O_3 (Escolaite around 16 %) and a very low concentration of $NiCr_2O_4$ oxides. Although the external oxide layer consisted of Cr_2O_3 oxide as a major phase, the presence of other

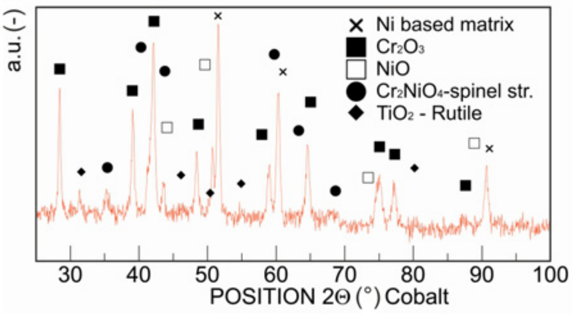

Fig. 10. Grazing incidence X-ray diffraction (GIXRD) spectrum obtained for oxide layers after oxidation test at 800°.

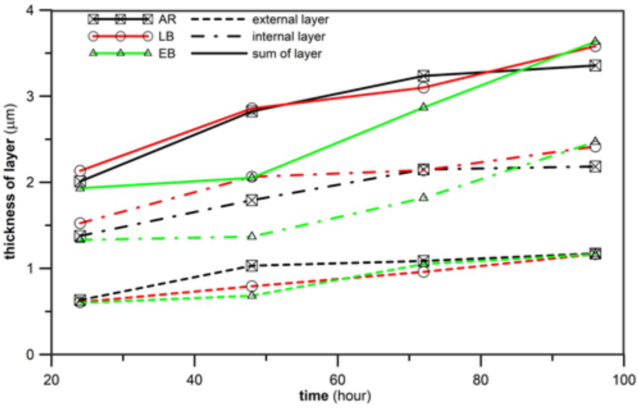

Fig. 11. The thickness of surface layers created during oxidation test.

oxides can be assumed according to EDS results. In literature, the presence of Cr_2O_3 and $NiCr_2O_4$ or also NiO is mainly discussed [31]. However, some studies also mentioned the presence of TiO_2 in the external oxide layer [31–33].

The more detailed investigation of the surface layers performed by Grazing Incidence X-ray diffraction (GI-XRD) analysis (Fig. 10) with a grazing incidence angle of 2° revealed other phases: Bunsenite (NiO) and Rutile (TiO_2). Also, the concentration distribution of the phases was changed. The major phase detected by GI-XRD was Cr_2O_3 (Escolaite; $\sim 51\,\%$). The other phases were $NiCr_2O_4$ ($\sim 14\,\%$), Rutile ($\sim 8\,\%$), Bunsenite ($\sim 5\,\%$). The remainder of the composition (to 100 wt.%) was determined to be the γ matrix.

According to EDS analysis, the internal layer consists of aluminum and oxygen, which most likely corresponds to Al_2O_3. The presence of Al_2O_3 was also confirmed by GI-XRD measurement. A layer consisting of $A1_2O_3$ was observed by Christ et al. [32] during an investigation on the kinetics and mechanisms of oxidation of Ni-based superalloys (IN 713 LC and IN 617). The presented results also correspond to the literature findings [9, 10, 34], where the oxidation behavior of the Ni-Cr-Al systems was studied.

The graph in Fig. 11 shows the changes in the thickness of the external, internal, and sum of the oxide layers for particular samples depending on the oxidation test duration. The same thickness of both the layers in 24 and 96 hours was measured; however, their thickness differs in time of exposure.

The external oxide layer, formed of Cr_2O_3 and $NiCr_2O_4$ oxides, was growing faster on the AR sample when compared to the EB and LB samples exhibiting the same layer growth rate. After 96 hours of exposition for all materials under investigation, the layer exhibits a thickness slightly above one micrometer (from 1.16 µm for EB sample to 1.17 µm for AR sample).

Faster growth of the internal $A1_2O_3$ oxide layer was observed for AR and LB samples compared to EB samples. However, at the end of the test, the thickness of layers for EB and LB samples was very similar to AR (EB = 2.46 µm, LB = 2.41 µm, AR = 2.18 µm). The observation was in agreement with the EDS surface mapping (Fig. 9) when AR and LB samples contained a higher amount of Al compared to the EB sample.

The thickness of the whole layer (internal + external) was comparable for AR and LB samples during the entire measurement. The layer was growing faster on AR and LB samples in comparison with the EB samples. On the other hand, comparable thickness of the whole layer was measured for all samples after 96 hours of oxidation test, see Fig 11. The higher thickness of Al_2O_3 on the LB samples during the testing, compared to the EB samples, can be explained via faster growth of the internal layer due to the higher content of the Al in the LB sample surface layer. The lower content of Cr in the LB sample surface layer deteriorates the growth of the external oxide layer and allows the reaction of O with Al. After 48 hours of oxidation, the internal layer creation on the LB sample was saturated. The external layer was growing linearly on the LB sample.

The lower content of Al measured for the EB sample resulted in slowlier internal Al_2O_3 oxide layer creation compared to the other samples. On the other hand, the oxidation time prolongation accelerates the oxidation, and the oxide layers started to grow more significantly also on the EB sample. After 96 hours of the test, a comparable whole layer thickness for all the samples was measured. EB and LB samples exhibited slightly higher layer thickness than AR samples.

4. Conclusions

Structural changes occurring due to the surface laser and electron beam treatment of IN 713LC Ni-based superalloy were examined.

Surface morphology changed after treatment due to the remelting of the surface layer. EB treatment resulted in higher surface roughness; however, a smaller amount of cracks on the treated sample surface was observed compared to the LB treatment. As a consequence of EB treatment, a homogeneous remelted zone (30–43 µm) consisting of the columnar dendritic structure was achieved, while LB treatment resulted in cellular-dendritic non-homogeneous (semi-circular track) remelted zone (22–86 µm).

A comparable increase of microhardness was measured on the treated samples surfaces (approx. 450 HV0.001) compared to the AR sample (approx. 325 HV0.001).

As a result of the treatment, a slightly different surface oxide layer creation was observed. Nevertheless, comparable oxide layer thickness was measured on all samples after 96 hours of oxidation (approx. 3.6 µm for EB and LB samples, 3.4 µm for AR sample).

Both the treatments influenced the superalloy microstructure and surface morphology. Even though the oxidation resistance was slightly different for the studied alloy states, the treatment did not deteriorate material resistance. So, the more homogeneous and less defected surface layer created due to the EB treatment, also increasing material microhardness, can be considered as favorable for the IN 713LC Ni-based superalloy surface properties.

Acknowledgements

This research was financially supported by the project CZ.01.1.02/0.0/0.0/19_262/0020138 of the Ministry of Industry and Trade of the Czech Republic. The equipment of research infrastructure CEITEC was used during the research activities.

The authors would like to thank Pavla Roupcová for her help with the XRD measurements. The authors appreciate the laser treatment (Marek Vostřák from New Technologies – Research Centre, University of West Bohemia, Pilsen) and electron beam treatment of the materials (Jan Kouřil from NETME Centre, Brno University of Technology, Brno).

References

[1] M. Šmíd, M. Petrenec, J. Polák, K. Obrtlík, A. Chlupová, Analysis of the effective and internal cyclic stress components in the Inconel superalloy fatigued at elevated temperature, Adv. Mat. Res. 278 (2011) 393–398. doi:10.4028/www.scientific.net/AMR.278.393

[2] M. J. Donachie, S. J. Donachie, Superalloys: A Technical Guide. 2nd ed., ASM International, 2002. ISBN 0-087170-749-7

[3] V. Horník, M. Šmíd, P. Hutař, L. Kunz, K. Hrbáček, Interaction of creep and high cycle fatigue of IN 713LC superalloy, Solid State Phenom. 258 (2017) 595–598. doi:10.4028/www.scientific.net/SSP.258.595

[4] L. Kunz, P. Lukáš, R. Konečná, S. Fintová, Casting defects and high temperature fatigue life of IN 713LC superalloy, Int. J. Fatigue 41 (2012) 47–51. doi:10.1016/j.ijfatigue.2011.12.002

[5] K. Obrtlík, S. Hutařová, L. Čelko, M. Juliš, T. Podrábský, I. Šulák, Effect of thermal barrier coating on low cycle fatigue behavior of cast Inconel 713LC at 900 °C, Adv. Mat. Res. 891–892 (2014) 848–853. doi:10.4028/www.scientific.net/amr.891-892.848

[6] I. Šulák, K. Obrtlík, L. Čelko, T. Chráska, D. Jech, P. Gejdoš, Low cycle fatigue performance of Ni-based superalloy coated with complex thermal barrier coating, Mater. Charact. 139 (2018) 347–354. doi:10.1016/j.matchar.2018.03.023

[7] S. Hutařová, M. Juliš, K. Obrtlík, M. Kianicová, T. Podrábský, O. Dvořáček, The study of microstructure and properties of Al diffusion coating on Inconel 713LC, Key Eng. Mater. 465 (2011) 282–285. doi:10.4028/www.scientific.net/kem.465.282

[8] K. Obrtlík, S. Hutařová, M. Juliš, T. Podrábský, J. Polák, Low cycle fatigue behavior of cast superalloy Inconel 713LC with Al coating at 800 °C, Key Eng. Mater. 452–453 (2010) 265–68. doi:10.4028/www.scientific.net/KEM.452-453.265

[9] J. L. Smialek, G. H. Meier, High-temperature Oxidation, Wiley-Interscience, in: Ch. T. Sims, N. S. Stoloff, W. C. Hagel (Eds.), Superalloys II – High Temperature Materials for Aerospace and Industrial Power, John Wiley and Sons 1987, pp. 293–326. ISBN: 978-0-471-01147-7

[10] T. N. Rhys-Jones, Protective oxide scales on superalloys and coatings used in gas turbine blade and vane applications, Mater. Sci. Technol. 4 (1988) 421–430. doi:10.1179/mst.1988.4.5.421

[11] M. Lachowicz, W. Dudziński, K. Haimann, M. Podrez-Radziszewska, Microstructure transformations and cracking in the matrix of γ-γ' superalloy Inconel 713C melted with electron beam, Mater. Sci. Eng. A 479 (2008) 269–276. doi:10.1016/j.msea.2007.06.064

[12] A. T. Egbewande, R. A. Buckson, O. A. Ojo, Analysis of laser beam weldability of Inconel 738 superalloy, Mater. Charact. 61 (2010) 569–574. doi:10.1016/j.matchar.2010.02.016

[13] M. Montazeri, F.M. Ghani, O. A. Ojo, Heat input and the liquation cracking of laser welded IN738LC superalloy, Weld. J. 92 (2013) 258–264.

[14] M. Gäumann, S. Henry, F. Cléton, J.-D. Wagnière, W. Kurz, Epitaxial laser metal forming: Analysis of microstructure formation, Mater. Sci. Eng. A 271 (1999) 232–241. doi:10.1016/S0921-5093(99)00202-6

[15] B. S. Yilbas, H. Ali, N. Al-Aqeeli, C. Karatas, Laser treatment of Inconel 718 alloy and surface characteristics, Opt. Laser Technol. 78 (2016) 153–158. doi:10.1016/j.optlastec.2015.11.006

[16] J. Matlák, P. Doležal, J. Zapletal, F. Vančura, I. Dlouhý, Electron beam surface quenching of X37CrMoV51 tool steel swages, Manuf. Technol. 16 (2016) 744–749. doi:10.21062/ujep/x.2016/a/1213-2489/MT/16/4/744

[17] S. A. David, S. S. Babu, J. M. Vitek, Welding: Solidification and microstructure, JOM 55 (2003) 14–20. doi:10.1007/s11837-003-0134-7

[18] H. T. Mallikarjuna, W. F. Caley, N. L. Richards, The effect of cooling rate on the γ' composition, morphology and corrosion behaviour of IN738LC, Corros. Sci. 149 (2019) 37–44. doi:10.1016/j.corsci.2018.12.036

[19] R. K. Sidhu, O. A. Ojo, M. C. Chaturvedi, Microstructural analysis of laser-beam-welded directionally solidified INCONEL 738, Metall. Mater. Trans. A 38 (2007) 858–870. doi:10.1007/s11661-006-9063-8

[20] Y. Q. Chen, E. Francis, J. Robson, M. Preuss, S. J. Haigh, Compositional variations for small-scale gamma prime (γ') precipitates formed at different cooling rates in an advanced Ni-based superalloy, Acta Mater. 85 (2015) 199–206. doi:10.1016/j.actamat.2014.11.009

[21] M. B. Lachowicz, W. Dudziński, Characteristics of GTA fusion zones and heat affected zones in superalloy 713C, Mater. Sci-Pol. 30 (2012) 159–169. doi:10.2478/s13536-012-0023-2

[22] E. Chauvet, P. Kontis, E. A. Jägle, B. Gault, D. Raabe, C. Tassin, J. J. Blandin, R. Dendievel, B. Vayre, S. Abed, G. Martin, Hot cracking mechanism affecting a non-weldable Ni-based superalloy produced by selective electron beam melting, Acta Mater. 142 (2018) 82–94. doi:10.1016/j.actamat.2017.09.047

[23] S. Kou, Solidification and liquation cracking issues in welding, JOM 55 (2003) 37–42. doi:10.1007/s11837-003-0137-4

[24] M. K. Keshavarz, S. Turenne, A. Bonakdarc, Solidification behavior of Inconel 713LC gas turbine blades during electron beam welding, J. Manuf. Process. 31 (2018) 232–239. doi:10.1016/j.jmapro.2017.11.021

[25] X. Zhang, H. Chen, L. Xu, J. Xu, X. Ren, X. Chen, Cracking mechanism and susceptibility of laser melting deposited Inconel 738 superalloy, Mater. Des. 183 (2019) 108105. doi:10.1016/j.matdes.2019.108105

[26] T. DebRoy, A. David, Physical processes in fusion welding, Rev. Mod. Phys. 67 (1995) 85–112. doi:10.1103/RevModPhys.67.85

[27] S. Petronic, S. Drecun-Nesic, A. Milosavljevic, A. Sedmak, M. Popovic, A. Kovacevic, Microstructure changes of nickel-base superalloys induced by interaction with femtosecond laser beam, Acta Phys. Pol. A 116 (2009) 550–552. doi:10.12693/APhysPolA.116.550

[28] C. Chan, J. Mazumder, One-dimensional steady state model for damage by vaporization and liquid expulsion due to laser-material interaction, J. Appl. Phys. 62 (1987) 4579–4586. doi:10.1063/1.339053

[29] T. Liu, L. J. Yang, H. L. Wei, W. C. Qiu, T. Debroy, Composition change of stainless steels during keyhole mode laser welding, Weld. J. 96 (2017) 258–270.

[30] Y.-J. Liang, H.-M. Wang, Origin of stray-grain formation and epitaxy loss at substrate during laser surface remelting of single-crystal nickel-base superalloys, Mater. Des. 102 (2016) 297–302. doi:10.1016/j.matdes.2016.04.051

[31] J. L. Smilek, P. J. Bonacuse: Compositional effects on the cyclic oxidation resistance of conventional superalloys, Mater. High Temp. 33 (2016) 489–500. doi:10.1080/09603409.2016.1160501

[32] H. J. Christ, L. Berchtold, H. G. Sockel, Oxidation of Ni-base alloys in atmospheres with widely varying oxygen partial pressures, Oxid. Met. 26 (1986) 45–76. doi:10.1007/BF00664273

[33] H. Wei, G. C. Hou, X. F. Sun, H. R. Guan, Z. Q. Hu, Oxidation behavior of a cast polycrystalline Ni-base superalloy in air: At 900 and 1000 °C, Oxid. Met. 68 (2007) 149–163. doi:10.1007/s11085-007-9066-x

[34] P. Lv, X. Sun, J. Cai, C. Zhang, X. Liu, Q. Guan, Microstructure and high temperature oxidation resistance of nickel based alloy GH4169 irradiated by high current pulsed electron beam, Surf. Coat. Technol. 309 (2017) 401–409. doi:10.1016/j.surfcoat.2016.11.041